COMMUNICATION

Additive-induced Miscibility Regulation~~Control~~ and Hierarchical Morphology Enables 17.5% Binary Organic Solar Cells

Received 00th January 20xx,
Accepted 00th January 20xx

DOI: 10.1039/x0xx00000x

Jie Lv, ‡[a,b] Hua Tang,‡[a,b,c] Jiaming Huang, [c] Cenqi Yan, [c] Kuan Liu, [c] Qianguang Yang,[a,b] Dingqin Hu, [a] Ranbir Singh, [d] Jawon Lee,[e] Shirong Lu, *[a] Gang Li, *[c] & Zhipeng Kan *[a]

Due to the barrierless free charge generation, low charge trapping, and high charge mobilities, the PM6:Y6 organic solar cell (OSC) achieves excellent power conversion efficiency (PCE) of 15.7%. However, the deficient hole transfer from Y6 to PM6 limits the further enhancement of the device performance. Herein, we demonstrate an additive-induced miscibility and morphology control strategy to achieve the balance of exciton dissociation and charge collection, prompting the PCE of OSCs composed of PM6: Y6 from 15.7% to 17.5%, which stands the top PCE value of PM6: Y6 binary OSCs. The external quantum efficiency (EQE) of the optimal device significantly improves in the wavelength range where Y6 harvests photons. Therefore, the short circuit current density (J_{SC}) enhances to 26.98 mAcm^{-2}, achieving 94.4% of the maximum theoretical J_{SC} obtained from the identical device configuration. The remarkable performance enhancement mainly results from the miscibility-driven donor and acceptor phase optimization with hierarchical morphology formation, leading to the improved photon to electron response of the Y6 phase, enhanced and balanced charge extraction and collection. Our findings highlight the significance of morphology control towards unleashing the full potential of OSC materials.

Broader context

In the last decade, solution-processed bulk-heterojunction (BHJ) organic solar cells (OSCs) have drawn extensive attention from Physicists, Chemists, Materials Scientists, industrialization experts attributed to their short energy payback time, low carbon footprint, and facile manufacture into flexible, lightweight, and semitransparent devices. Tremendous efforts have been made in photoactive material designs, device engineering, and device physics, leading to the continually breakthrough in OSCs with power conversion efficiencies (PCEs) over 17%. However, the technique for reaching the full potential of the existing photoactive material is rarely studied. To this end, we report an additive-induced morphology manipulation strategy to unleash the full potential of the existing state-of-the-art photoactive materials, namely, 4,8-bis(5-(2-ethylhexyl)-4-fluorothiophen-2-yl)benzo[1,2-b:4,5-b`]- dithiophene (BDT-F) and 1,3-bis(thiophen-2-yl)-5,7-bis(2-ethylhexyl)benzo-[1,2-c:4,5-c`]dithiophene-4,8-dione (BDD) (PM6) and (2,20-((2Z,20Z)-((12,13-bis(2-ethylhexyl)-3,9-diundecyl-12,13-dihydro-[1,2,5]thiadiazolo[3,4-e]thieno[2,"30':4',50]thieno[20,30:4,5]pyrrolo[3,2-g]thieno[20,30:4,5]thieno[3,2-b]indole-2,10-diyl)bis(methanylylidene))bis(5,6-difluoro-3-oxo-2,3-dihydro-1H-indene-2,1-diylidene))dimalononitrile) (Y6). As a result, the PCEs of the PM6: Y6 devices boost from 15.7% to 17.5%, which prompt the PCE of this system to a bran-new level and highlight the importance of morphology control.

Introduction

Solution-processed bulk-heterojunction (BHJ) organic solar cells (OSCs) have emerged as an excellent rival for next-generation photovoltaic technology attributed to their short energy payback time, low carbon footprint, and facile manufacture into flexible, lightweight, and semitransparent devices.[1-10] The power conversion efficiencies (PCEs) of OSCs have been steadily rising in the past decade on account of the tremendous efforts in photoactive material designs, device engineering, and device physics.[11-13] Especially, the development of fused-ring electron acceptor Y6 pushed the PCE over 15% by pairing selected polymer donors.[14] To further enhance the photovoltaic performance, a series of Y6 derivatives have been synthesized and PCE for single-junction binary BHJ OSCs have exceeded 17%.[15] While the research focuses were usually concentrated on the advance of photoactive material structures, the strategies to further release the potential of the reported photovoltaic materials still far lag. Take the benchmark active layer PM6:Y6 as an example, the superior solar cells performance was attributed to the barrierless free charge generation, low charge trapping, and high charge mobilities. At the same time, the fast Y6 exciton decay led to deficient hole transfer from Y6 to PM6 compared to the electron transfer efficiency from PM6 to Y6, limiting the photovoltaic device performance.[16] This observation indicates that there are substantial opportunities for further efficiency enhancement by approaching its optimum

[a] Thin-film Solar Technology Research Center, Chongqing Institute of Green and Intelligent Technology, Chinese Academy of Sciences, Chongqing 400714, P. R. China. E-mail: lushirong@cigit.ac.cn ,kanzhipeng@cigit.ac.cn
[b] University of Chinese Academy of Sciences, Beijing 100049, P. R. China.
[c] Department of Electronic and Information Engineering, The Hong Kong Polytechnic University, Hung Hum, Kowloon, Hong Kong SAR, P. R. China. E-mail: gang.w.li@polyu.edu.hk
[d] Department of Energy & Materials Engineering, Dongguk University, Seoul 04620, Republic of Korea.
[e] Department of Chemical Engineering and Applied Chemistry, Chungnam National University, Daejeon, 34134, Republic of Korea
‡ Both authors contributed equally to this work.
Electronic Supplementary Information (ESI) available: [details of any supplementary information available should be included here]. See DOI: 10.1039/x0xx00000x

active layer morphology and full light-harvesting potential. Thus, developing the technique to fulfill the PCE growth on commercial photoactive material is of importance to the advance of OSCs.

Reaching the full potential of the existing state-of-the-art photoactive materials requires superior active layer morphology, including more suitable domain size, donor/acceptor (D/A) phase separation, and D/A interfaces to ensure improved exciton dissociation, and more reasonable crystallinity as well as domain purity for the achievement of enhanced charge transport.[17-19] In this scenario, the miscibility of the donor and acceptor is a key factor to determine the quality of such morphology.[20-22] Generally, low miscibility can be considered as the driving force of phase segregation, which tends to form large and pure domains that facilitate charge transport. On the contrary, high miscibility offers a low driving force for phase separation, which tends to deliver small and impure domains that aid exciton dissociation. Thus, balanced exciton dissociation and charge transport can be obtained through miscibility-driven phase separation control. The miscibility of the donor and acceptor is estimated by the Flory – Huggins interaction parameter χ, and it can be either calculated by the melting - point depression method or obtained from the equation of $K\left(\gamma_{donor}^{1/2}-\gamma_{acceptor}^{1/2}\right)^2$, where *K* is a positive constant,[23, 24] γ_{donor} and $\gamma_{acceptor}$ are the surface energy values of donor and acceptor calculated from the contact angle measurements, respectively.[23, 25, 26] When the melting-point depression method was applied, free standing films with various donor/acceptor contents were measured with differential scanning calorimetry and approximations were applied during the calculation. To reduce the materials consumption in melting-point depression method and avoid approximation, the contact angle measurements based method was more widely adopted.

To date, a few avenues have been proven effective to fine-tune the miscibility towards optimal morphology: i) the modification of photoactive materials; ii) the construction of ternary OSCs. The first approach was widely applied to achieve efficient OSCs. Cao group designed a series of polymeric donors with different side chains, namely PTAZ-TPD10-Cn (n = 6, 8, 10). The miscibility of the donor and $PC_{71}BM$ increased with the lengthened side chains; as a comparison, N2200- and ITIC-based blends show an opposite trend. Lower-miscibility TPD10-Cn: acceptor system exhibited more intermixed morphology, contracted domains, and favorable vertical phase distribution. As a result, PTAZ-TPD10-C6: $PC_{71}BM$, PTAZ-TPD10-C10: N2200, and PTAZ-TPD10-C10: ITIC can achieve the optimal efficiencies of 6.3%, 6.8%, and 8.8%, respectively.[27] Recently, Li group reported a series of D-A1-D-A2 type terpolymer donors via a random ternary polymerization strategy by incorporating 0%, 20%, 50%, and 100% content of thiophene-thiazolothiazole (TTz) building block into the skeleton of the state-of-the-art polymer (PM6). They found that the surface energies of the polymer reduced gradually with the growing content of TTz. PM1 with 20% TTz incorporation possesses the optimum D/A miscibility, which results in the appropriate phase separation and phase purity and contributes to the excellent fill factor (FF) of 78% and PCE of 17.6%.[28] Introducing the third component is another viable mean to fine-tuning the miscibility. Baran demonstrated the practice by replacement of 30% host non-fullerene acceptor (NFA) IDTBR with IDFBR, which has higher miscibility with P3HT. The partial incorporation of IDFBR thus reduced the phase separation in the corresponding device, which leads to the enhanced charge transfer and the improved short-circuit current density (J_{SC}) and FF. Consequently, P3HT: IDTBR: IDFBR obtained a PCE of 7.7%, higher than the PCE of P3HT: IDTBR (6.3%).[29] For another instance, to improve the performance of all-small-molecule (ASM) BTR-Cl: Y6 devices, fine regulation of the miscibility via incorporating fullerene derivatives as the third component was reported. According to the surface energies, it was found that the miscibility of $PC_{71}BM$/Y6 and BTR-Cl/$PC_{71}BM$ is higher than that of BTR-Cl/Y6, which leads to a better mixed D/A phase with a more reasonable domain size contributing to charge separation. PCE of 15.34% and FF of 77.11% in ASM OSCs have validated effective of the miscibility-driven morphology manipulation approach.[30] Nevertheless, considerable efforts are indeed required either in the chemical synthesis or in the selection of the third component, and more straightforward approaches to control the miscibility of commercial organic semiconductors to optimize the OSCs have rarely been reported.

Herein, a simple yet effective additive-induced miscibility control approach towards superior morphology is introduced to further release the potential of the state-of-the-art commercial polymer donor: acceptor system (PM6 and Y6). The solvent additive 1-chloronaphthalene (CN) has been the most reported

Table 1. Photovoltaic performance of PM6: Y6-based OSCs processed with varied solvent additives under simulated AM1.5G illumination (100 mW cm^{-2}).

Active layer	Solvent additive [a]	V_{OC} [V]	J_{SC} [mA cm^{-2}]	*Calc.* J_{SC} [mA cm^{-2}]	FF [%]	PCE [b] [%]	$\chi_{donor-acceptor}$ [c] (×10^{-2} K)
PM6:Y6	NA	0.85(0.84±0.01)	24.99(24.55±0.44)	24.06	70.6(69.7±0.9)	15.0(14.5±0.5)	4.65
	0.9 vol% FN	0.83(0.83±0.02)	26.98(26.73±0.22)	26.31	77.8(75.8±1.9)	17.5(16.9±0.6)	10.98
	0.5 vol% CN	0.84(0.83±0.02)	25.79(25.55±0.24)	24.91	71.9(70.5±1.4)	15.7(15.1±0.6)	53.13
	0.6 vol% BN	0.84(0.84±0.02)	26.00(25.86±0.14)	25.40	74.9(74.0±0.9)	16.4(16.1±0.3)	6.76

[a] The vol% is represents volume percent.

[b] The average values obtained from 13 devices.

[c] Estimates for Flory–Huggins interaction parameter ($\chi_{donor-acceptor}$), which is derived, in principle, from the relation of $K\left(\gamma_{donor}^{1/2}-\gamma_{acceptor}^{1/2}\right)^2$.

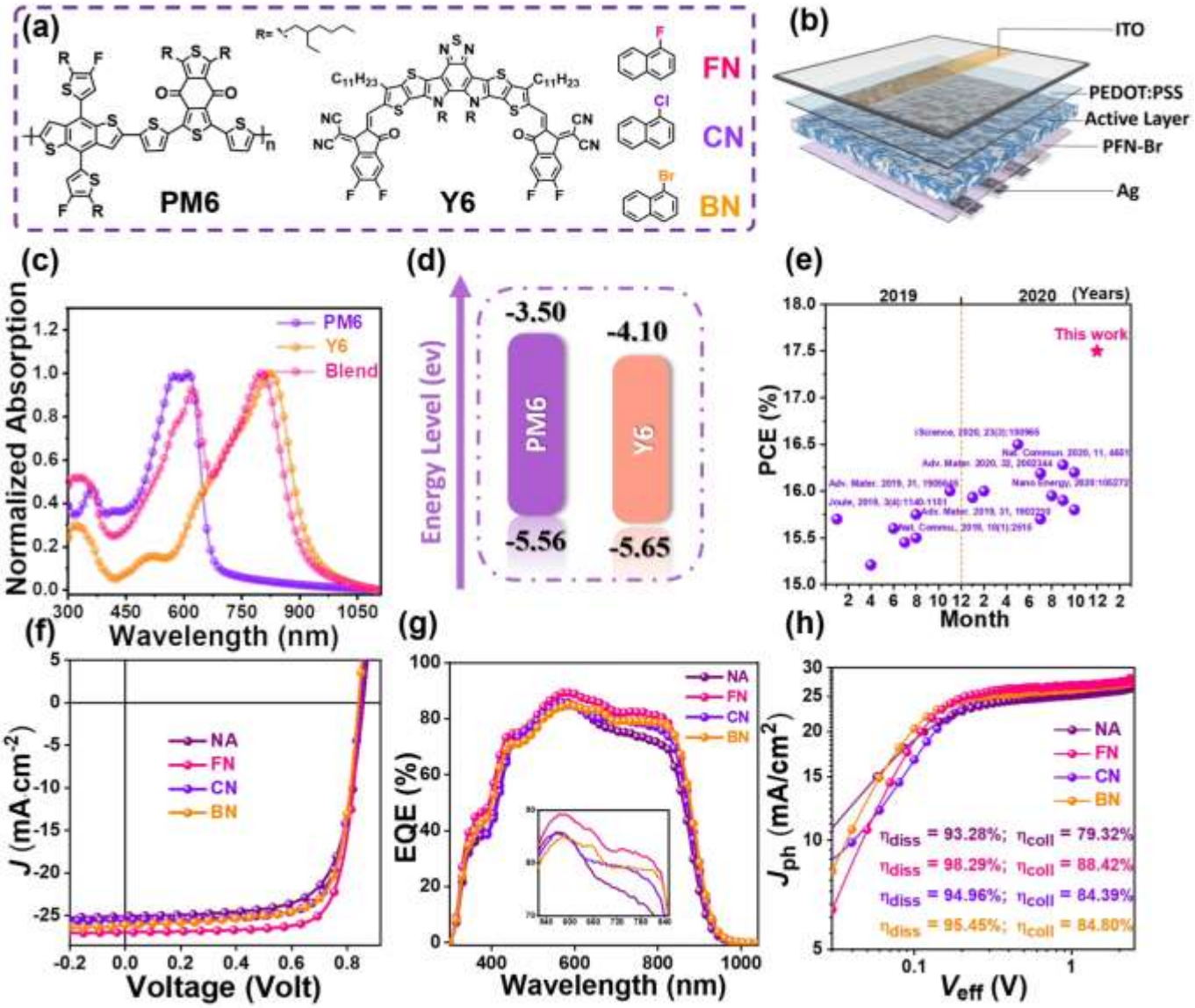

Figure 1. (a) Molecular structures of PM6 and Y6, and additives of FN, CN, and BN. (b) Device architecture. (c) Normalized thin film UV-vis absorbance spectra of PM6, Y6, and PM6: Y6 blend. (d) Energy level diagram of PM6 and Y6. (e) Summary of the PCE based on reported single-junction binary PM6:Y6 BHJ OSCs. (f) *J-V* characteristics of devices processed with NA, FN, CN, and BN. (g) EQE spectra (Scale-up EQE spectra of 525-830 nm) and (h) photocurrent density (J_{ph}) as a function of the effective voltage (V_{eff}) of the optimized OSCs.

to fine-tune the morphology of PM6: Y6 OSC yielding enhanced 15.7% efficiency compared to its non-additive (NA) counterpart (15%). In this work, we explored the effect of solvent additives by replacing the halogen element Cl in CN molecule with F and Br, namely 1-Fluoronaphthalene (FN) and 1-Bromonaphthalene (BN).[31, 32] We found surprisingly that the halogen element can have significant influence on the morpholoty fine-tuning: FN-induced medium miscibility of PM6/Y6 led to optimal phase separation with champion exciton dissociation efficiency of 98.29% and PCE of 17.5%; CN-induced low miscibility of D/A resulted in excessive phase separation with reduced exciton dissociation efficiency of 94.96% and PCE of 15.7%; BN-induced high miscibility of D/A caused insufficient phase segregation with relatively low exciton dissociation efficiency of 95.45% and PCE of 16.4%. It is worth noting that the 17.5% efficiency achieved by the FN-induced miscibility control strategy stands the champion PCE value of PM6: Y6 binary OSCs. The improved photon to electron response of the Y6 phase leads to enhanced photocurrent density to 26.98 mAcm^{-2}, which is 94.4% of the maximum theoretical photocurrent density obtained from optical simulations. In addition, the remarkable enhancement of FF from 70.6% (NA) to 77.8% (FN) soundly proves the effectiveness of this approach on delicate morphology manipulation, which also paves an avenue to further release the potential of existing OSC systems.

Result and Discussion

The optoelectronic properties of PM6:Y6 and the solvent additives used in this work are presented in **Figure 1**. The molecular structures of PM6, Y6, and additives of FN, CN, and BN are shown in **Figure 1a**. **Figure 1b** depicts the photovoltaic

device architecture that obtained a PCE of 15.7%. **Figure 1c** presents normalized UV-vis absorbance spectra of neat films of PM6 and Y6, and blend film of PM6: Y6. The absorption maxima of PM6 and Y6 films are at 609 and 826 nm, which are capable of possessing complementary photon absorption. PM6 and Y6 film exhibit absorption onsets of 677 and 932 nm, respectively, which account for the respective optical bandgaps of 1.83 and 1.33 eV. **Figure 1d** displays the energy level diagram of PM6 and Y6. PM6 possesses the lowest unoccupied molecular orbital (LUMO) level of -3.50 eV and the highest occupied molecular orbital (HOMO) level of -5.56 eV, which matches well with Y6 (-4.10 eV/ -5.65 eV).

Prior to discussing the experimental performance of the devices, we performed a transfer matrix model simulation to get the maximum theoretical short circuit current density. The refractive index and extinction coefficient of the active layer were determined by ellipsometry measurements, and samples were prepared following the reported procedure.[33, 34] When unity internal quantum efficiency and identical device configuration (**Figure 1b**) was used in the simulation, the maximum short circuit current density of 28.58 mA cm^{-2} was obtained, i.e., the full photocurrent density potential of such devices. (details in **Figure S3~S5**) Next, the performance of the BHJ devices was optimized by varying the additives to fine-tune the miscibility of the PM6/Y6 phase toward enhanced device performance. (**Table S1-S5**) **Table 1** summarizes the figures of merit of the PM6: Y6-based devices subject to different additives under simulated AM1.5G irradiation (100 mW cm^{-2}). Figure 1e summarizes the reported work with the champion PCE based on binary PM6:Y6 BHJ OSCs. To the best of our knowledge, this FN-induced miscibility control strategy prompt the PCE of the binary PM6:Y6 BHJ OSCs to a bran-new level. **Figure 1f** depicts the current density-voltage (*J-V*) characteristics of NA, FN, CN, and BN-based devices. The active layer of control NA-based device shows a low $\chi_{donor-acceptor}$ value of 4.65×10^{-2}K, implying a very high miscibility of PM6/Y6, which results in a PCE of 15.0% with a J_{SC} of 24.99 mA cm^{-2} and a FF of 70.6%. The introduction of CN significantly improves the $\chi_{donor-acceptor}$ value to 53.13×10^{-2}K, inferring dramatically decreased miscibility of PM6/Y6, leading to the slightly enhanced device performance of 15.7% efficiency with a J_{SC} of 25.79 mA cm^{-2} and a FF of 71.9%, which is also in accordance with the reported work.[14] When changing the solvent additive to BN, the corresponding active layer has obtained $\chi_{donor-acceptor}$ value of 6.76×10^{-2}K and increased device performance of 16.4% efficiency with a J_{SC} of 26.00 mA cm^{-2} and a FF of 74.9%. The obvious enhanced PCE of BN-based device with slightly changed $\chi_{donor-acceptor}$ value compares to the NA-based counterpart indicates fine-tune the miscibility of PM6/Y6 is of significance to boost the device performance.[20, 34] The utilization of FN has obtained the $\chi_{donor-acceptor}$ value of 10.98×10^{-2}K with a remarkably enhanced photovoltaic performance of 17.5% efficiency with a J_{SC} of 26.98 mA cm^{-2} and a FF of 77.8%. The miscibility of the FN-based BHJ active layer is between CN and BN-based counterparts, meaning the medium miscibility is preferential for achieving the top-performing PM6: Y6-based OSCs. In addition, the J_{SC} of FN based device reached 94.4% of the maximum short circuit current density, which is clearly higher than those obtained from devices with other processing conditions. These results prove the effectiveness of further improving the photovoltaic performance of commercial photoactive materials via additive-induced miscibility/morphology manipulation strategy.

Figure 1g presents the external quantum efficiency (EQE) spectra of the NA, FN, CN, and BN-based devices. The EQE curves of all the four devices are very similar in shape, however, the FN exhibits a stronger photon to electron response than those of the NA, CN, and BN devices in the range of 340-830 nm, which contributes to the enhanced J_{SC}. The EQE maximum of the FN based device is 89.3%, obviously higher than the NA device of 85.8%, CN device of 85.3%, and BN device of 84.9%. It is worth mentioning that the FN-induced miscibility control strategy remarkably increases the EQE from 525-830 nm, which means the FN-induced medium miscibility of the PM6/Y6 can trigger the photon to electron response from the Y6 phase. The J_{SC} values of the NA, FN, CN, and BN-based BHJ devices integrated from the EQE spectra are 24.06, 26.31, 24.91, and 25.40 mA cm^{-2}, respectively, consistent with the J_{SC} values measured from the solar simulator (within a 2.5% error of FN and BN-based BHJ devices, within a 3.4% error of NA and CN-based BHJ devices, **Table 1**).

The photocurrent density (J_{ph}) as a function of the effective voltage (V_{eff}) was plotted to study the charge generation and extraction properties (**Figure 1h**). $J_{ph} = J_L - J_D$, in which J_L is the current density under illumination and J_D is that in the dark. $V_{eff} = V_0 - V_A$, where V_0 is the voltage when J_{ph} is equal to 0, and V_A is the applied bias voltage. At a high V_{eff} of 2.5 V, the gross photogenerated excitons are assumed to be dissociated into free charge carriers and then collected by electrodes. The FN-based BHJ device exhibits a saturated current density (J_{sat}) of 27.45 mA cm^{-2}, higher than the NA (26.79 mA cm^{-2}), CN (27.16 mA cm^{-2}), and BN-based BHJ devices (27.24 mA cm^{-2}), which is in line with the photon harvest capability of these four blends. The exciton dissociation efficiency ($\eta_{diss} = J_{SC}/J_{sat}$) and charge collection efficiency ($\eta_{coll} = J_{max\ power}/J_{sat}$) were calculated under the short-circuit and maximum power output conditions, respectively.[35] The FN-based device exhibits a η_{diss} of 98.29% and a η_{coll} of 88.42%, higher than those of the NA (η_{diss} of 93.28% and η_{coll} of 79.32%), CN (η_{diss} of 94.96% and η_{coll} of 84.39%) and BN-based device (η_{diss} of 95.45% and η_{coll} of 84.80%), indicating FN-induced miscibility control maximizes and balances exciton dissociation and charge collection to release the full potential of the PM6: Y6 OSCs.

The above analysis indicates that the key factor governing the high performed FN-based device originates from the optimal morphology control, and therefore, we turned to check the detail changes in thin films with and w/o solvent additives. Time-resolved in-situ UV–vis absorption measurements (**Figure 2a-d**) are performed to unveil the absorption transformation under the optimal posttreatment condition (thermal annealing at 110℃ for 10 min) for the PM6:Y6 system. We have shown that NA, CN, and BN-based blend films all exhibit an obvious and sharp absorption transformation on the Y6 phase between 5-10s, however, FN-based blend film presents a smooth red-shifted absorption transformation on the Y6 phase which is

attributed to the FN-induced miscibility manipulation, which slows down the crystallization. The fast crystallization normally results in relatively irregular orientation and more defects. Thus, the FN-based blend film shows stronger photon harvest capacity on the Y6 phase, which is accounts for the EQE (525-830 nm) enhancement. The corresponding absorption spectra under TA of 0 and 45s are shown in **Figure S6**.

Grazing-incidence wide-angle X-ray scattering (GIWAXS) was carried out to study the molecular packing and orientation in the thin films, and the corresponding GIWAXS parameters are summarized in **Table S6**. The additives have different impacts on PM6 and Y6 neat films. The additives of FN, CN, and BN increasingly improve the crystallinity of PM6 (**Figure S7**), however, FN-induced Y6 neat film obtains high crystallinity, BN- and CN-induced Y6 neat film obtains medium and low crystallinity **(Figure S7)**. For the blend films processed by different additives, all the BHJ blend films demonstrate similar molecule orientation. (**Figure 2e-h**) The FN-based BHJ film with

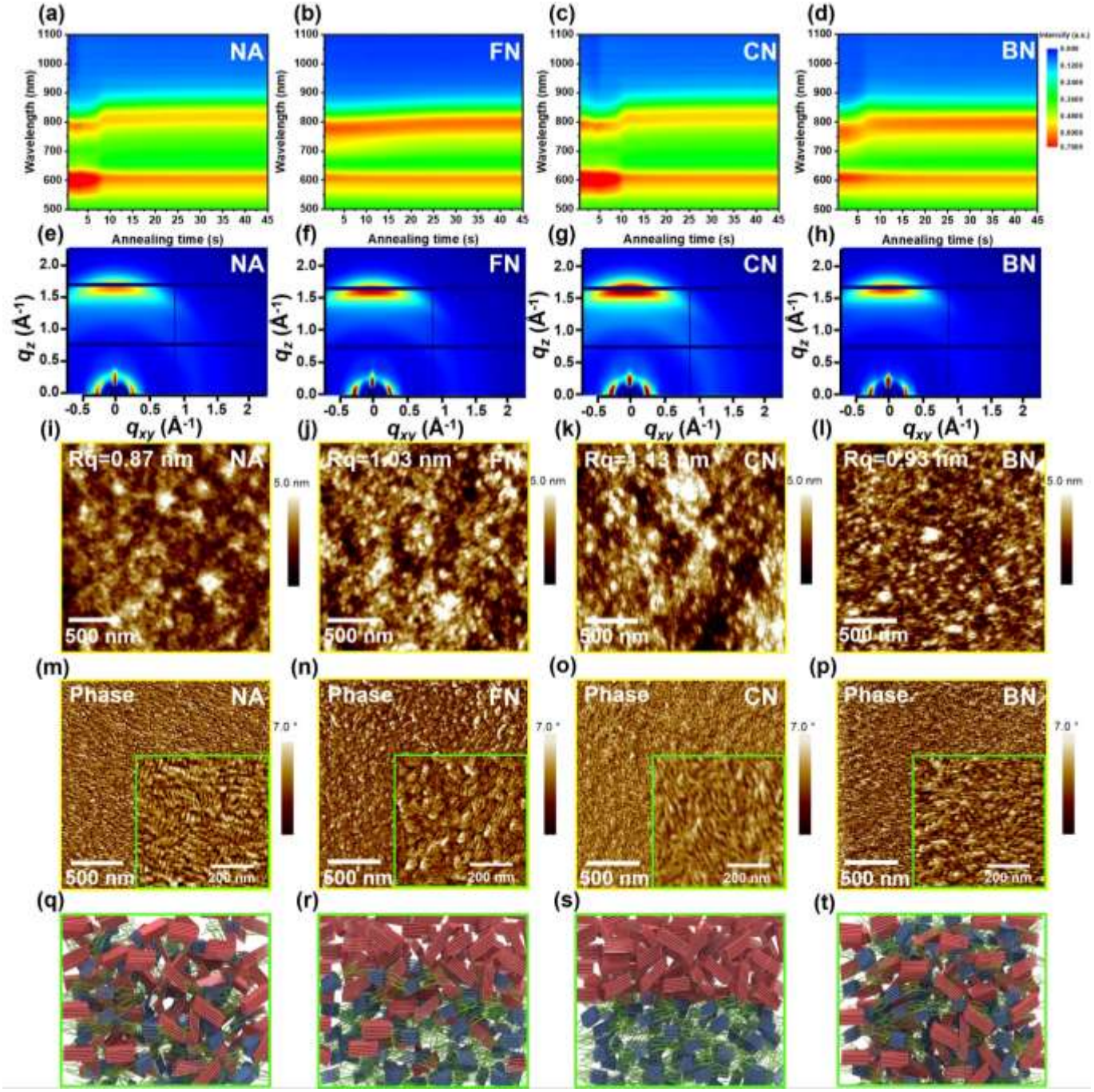

Figure 2. Time-resolved in-situ UV–vis absorption of optimized blend films of (a) NA, (b) FN, (c) CN, (d) BN under thermal annealing at 100 ℃. 2D GIWAX patterns of films based on PM6: Y6 blend of (e) NA, (f) FN, (g) CN, (h) BN. AFM height images of PM6: Y6 blend film of (i) NA, (j) FN, (k) CN, (l) BN. AFM phase images with scale up inset of PM6: Y6 blend film of (m) NA, (n) FN, (o) CN, (p) BN. The D/A interfaces schematic drawing of PM6: Y6 blend film of (q) NA, (r) FN, (s) CN, (t) BN.

medium miscibility of PM6/Y6 displays (100) lamellar peaks at q_{xy}≈ 0.32 Å^{-1} (coherence length (CCL) =5.33 nm) (**Figure 2f and Figure S8**). In comparison, the CN-based counterpart with low miscibility of PM6/Y6 exhibits (100) lamellar peaks at q_{xy}≈ 0.32 Å^{-1} (CCL = 7.96 nm) and the BN-based counterpart with high miscibility of PM6/Y6 presents the same peak at q_{xy}≈ 0.33 Å^{-1} (CCL=4.87 nm). The (010) π-π stacking depicts the identical tendency. (**Figure 2e-h and Figure S8**) The FN-based BHJ film exhibits (010) π-π peaks at q_z ≈ 1.69 Å^{-1} with CCL= 1.70 nm, whereas its CN analog exhibits q_z≈ 1.70 Å^{-1} with CCL=1.86 nm, and the BN analog displays q_z≈ 1.69 Å^{-1} with CCL=1.58 nm. Generally, high crystallinity results in strong phase aggregation with reduced D/A interface, whereas low crystallinity leads to weak phase aggregation with increased D/A interface.[34] The identical molecule orientation and the medium CCL of both lamellar and π-π peak in the FN-based BHJ film with medium miscibility of PM6/Y6 finely improve and balance the exciton dissociation (98.29%) and charge collection (88.42%) endowing the full potential of PM6: Y6 binary OSCs with 17.5% efficiency.

The PM6/Y6 phase separation in the BHJ active layer was investigated by atomic force microscopy (AFM) (**Figure 2i-p)** and transmission electron microscopy (TEM) **(Figure S10)**. As the AFM height images demonstrated, the FN-induced BHJ films with medium miscibility of PM6/Y6 have a root mean square roughness (R_q) values of 1.03 nm **(Figure 2j)**, which is smaller than its CN-induced counterpart with low miscibility of PM6/Y6 (**Figure 2k,** R_q = 1.13 nm), and larger than its BN-induced counterpart with high miscibility of PM6/Y6 (**Figure 2l,** R_q = 0.93 nm), implying that this additive induced miscibility manipulation approach can finely control the molecular aggregation, which is in line with the trend of crystallinity ascertained by GIWAXS test. **(Figure 2e-h, and Figure S7)** As the AFM phase images **(Figure 2m-p)** indicate, relative to the CN and BN-based BHJ films, the FN-based film exhibits a very interesting hierarchical morphology, in which clear fibril (polymer) structures can be seen to closely attach onto or even embedded into larger grain structures. We suspect this hierarchical morphology with both D-A phase purity and intimate contact may provide a more efficient model for charge separation and transport and becomes a critical factor to boost the photovoltaic performance of the PM6: Y6-based OSCs.[36-40] Similar to GIWAXS characterization, the solvent additives have different impacts on the PM6 and Y6 phases respectively. Only small variation can be found from the PM6 phase (**Figure S10**) with the R_q order of NA (0.80 nm) < FN (0.81 nm) < CN (0.83 nm) < BN (0.88 nm), whereas obvious difference can be discovered from the Y6 phase (**Figure S11**) with the R_q order of NA (1.29 nm) < CN (1.44 nm) < BN (1.95 nm) < FN (2.52 nm). The remarkably enhanced photon response of the Y6 phase may be originated from the significantly increased Y6 phase aggregation, which also supports the hierarchical morphology scenario mentioned above. The order of the PM6/Y6 blend phase aggregation is distinct from both pure PM6 and Y6 phase, meaning the solvent additive is the key to manipulate the miscibility of the PM6/Y6

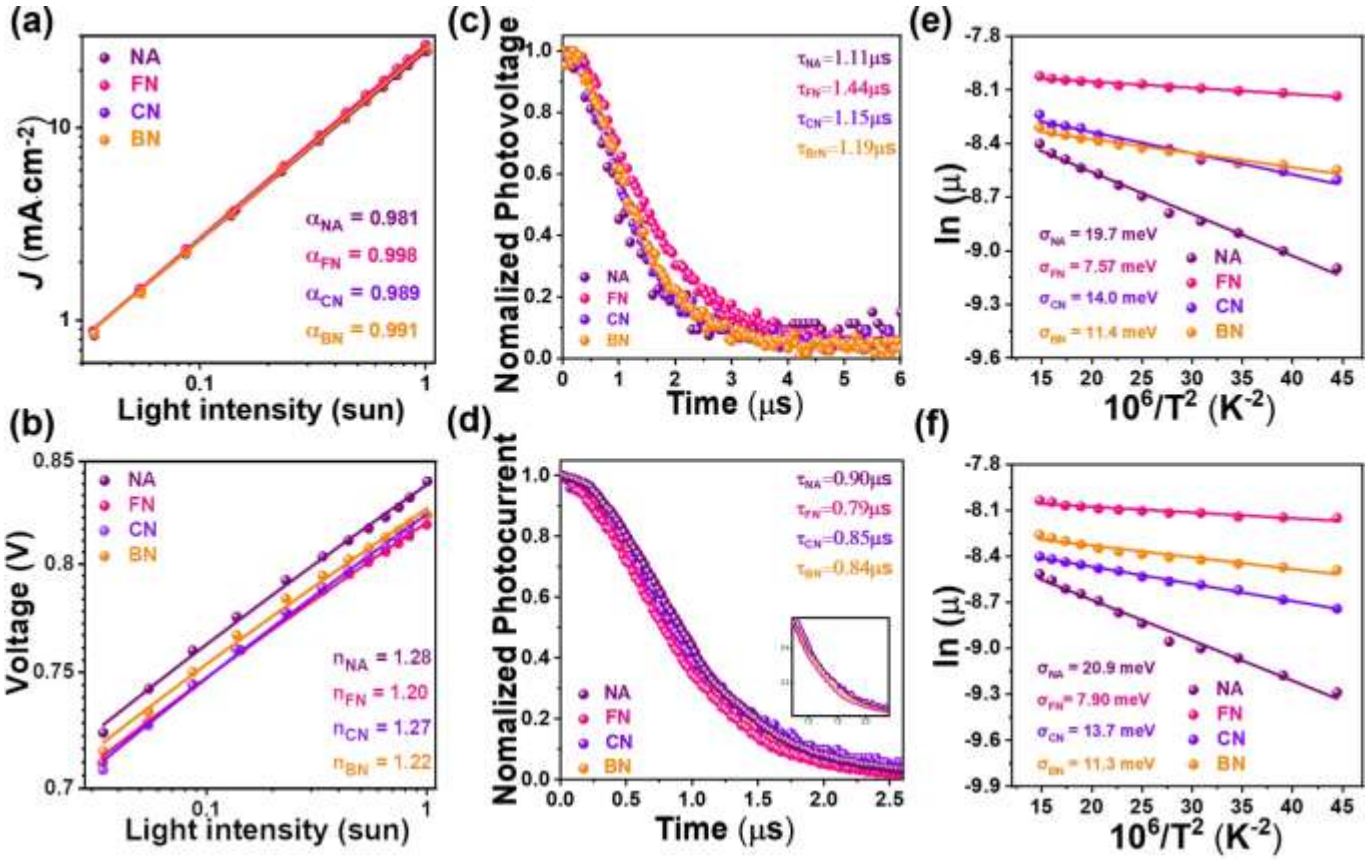

Figure 3 (a) J_{SC} versus P_{light} and (b) V_{OC} versus P_{light} of the PM6: Y6 devices processed with NA, FN, CN, and BN. (c) TPV and (d) TPC of the PM6: Y6 devices processed with NA, FN, CN, and BN. (e) zero-field hole mobility $\mu_{0,h}$, and (f) electron mobility $\mu_{0,e}$ versus $(1000/T)^2$.

for the enhanced and balanced exciton dissociation and charge collection.

Inspired by the morphology analysis, we proposed the schematic drawing of the D/A interfaces in **Figure 2q-t**. Owing to the least crystallinity and highest miscibility of PM6/Y6 in the NA based film, the two materials are well mixed but with less aggregation stacks as shown in **Figure 2q**; the medium miscibility and improved crystallinity of the active layer obtained from the film with FN is pictured in **Figure 2r**, which has proper mixed donor and acceptor at the D/A interfaces and continuous pure phase that ensures the exciton dissociation and charge transport; **Figure 2s** presents the D/A interface of CN processed PM6:Y6 with low miscibility and more pure domains, which should result in improved charge carrier mobilities; the slightly decreased miscibility of PM6/Y6 and improved crystallinity in the BN processed thin film can be observed in **Figure 2t**, indicating better exciton dissociation efficiency in comparison with the NA and CN processed films. These morphology data systematically unveil the nature of additive-induced miscibility control towards enhanced photovoltaic performance.

The distinct thin film morphologies directly influence the behavior of the free charge carriers in the devices, thus *J*–V curves under various incident light intensities, and the transient photovoltage/photocurrent (TPV/TPC) were performed.[41-43] Previous studies have reported that the bimolecular recombination losses could be qualitatively analyzed by employing the power-law relation of $J_{SC} \propto I^{\alpha}$ to fit J_{SC} as a function of the incident light intensity plotted in log scales.[44] In short, a value of α equal to unity reflects the extreme case where all the free carriers are swept out and collected at the electrodes before recombination. From fitting the data of J_{SC} vs. light intensity as illustrated in **Figure 3a**, α values of 0.981, 0.998, 0.989, and 0.991 were obtained for NA, FN, CN, and BN-based BHJ devices, respectively, which are indicative of negligible bimolecular recombination losses for all these systems. On the other hand, the presence of trap-assisted Shockley–Read–Hall (SRH) recombination can be distinguished from the ideality factor *n*. When the V_{OC} was plotted as a function of the incident light intensity (**Figure 3b**), the data follow the expression of $V_{OC} \propto nkT/qln(I)$, where *n*, k, T, and q are the ideality factor, Boltzmann constant, the temperature in Kelvin, and elementary charge, respectively.[44] In this case, it indicates the presence of trap-assisted recombination if the *n* value deviates from 1 (trap-free condition). The fitted data shown in **Figure 3b** presented *n* values of 1.28, 1.20, 1.27, and 1.22 for NA, FN, CN, and BN-based BHJ devices, indicating that the FN-induced medium miscibility of PM6/Y6 aiding this BHJ device suffers from the lowest trap-assisted recombination. These results reveal that finely manipulate the miscibility of PM6/Y6 via solvent additives can notably reduce the density of the trap-assisted recombination center, which accounts for the performance enhancement of PM6: Y6 devices.

Quantitative analysis of the charge recombination dynamics and extraction across BHJ active layers in devices were carried out by TPV and TPC characterizations. The carrier lifetimes (τ) under open-circuit conditions (**Figure 3c**) were extracted from the TPV decay dynamics employing mono-exponential fits under a 1 sun bias.[36, 45, 46] The FN-based BHJ device exhibits a τ value of 1.44 μs, longer than its NA, CN, and BN-based counterparts (1.11,1.15 and 1.19 μs), in conformity to the weaker recombination in FN-induced medium miscible device. In addition to charge recombination, charge extraction properties also play a key role. The competition between carrier sweep-out and recombination during the operation was obtained through the TPC measurement (**Figure 3d**). The photocurrent decay time under short-circuit conditions is 0.79 μs for the FN-based BHJ device, smaller than that for the NA (0.90 μs), CN (0.85 μs), and BN-based device (0.84 μs), illustrating that medium miscibility of PM6/Y6 in the BHJ device can effectively facilitate charge carrier extraction, which is in line with the aforementioned higher charge collection efficiency of 88.42% in the FN-based BHJ device (**Figure 1g**).

To unveil the charge transport process, both hole and electron carrier mobilities were estimated by fitting the space-charge-limited- current (SCLC) model.[47-50] Hole-only devices were fabricated with the structure of ITO/PEDOT:PSS/active layer/MoO_3/Ag and electron-only devices with ITO/ZnO/PFNBr/Active layer/ PFNBr /Ag. The FN-based device shows medium hole (5.24×10^{-4} cm^2 V^{-1} s^{-1}) and electron (5.28×10^{-4} cm^2 V^{-1} s^{-1}) mobilities, higher than the NA-based (4.08×10^{-4} and 2.63×10^{-4} cm^2 V^{-1} s^{-1}) and the BN-based device (4.66×10^{-4} and 4.46×10^{-4} cm^2 V^{-1} s^{-1}), but lower than the CN-based device (7.34×10^{-4} and 5.55×10^{-4} cm^2 V^{-1} s^{-1}). However, the hole and electron mobility are more balanced (μ_e/μ_h = 0.99), which may account for the higher FF of 77.8% in the FN-based BHJ devices. Additionally, the hole and electron energy disorder (σ_h and σ_e) can be obtained from temperature dependent mobility characterizations using the Gaussian disorder model (GDM):[51, 52]

$$\mu_0 = \mu_\infty exp\left\{-\left(\frac{4}{9}\right)\left[\frac{\boldsymbol{\sigma}^2}{(kT)^2}\right]\right\}$$

where k is the Boltzmann constant, T is the temperature, μ_0 is the zero-field mobility, and μ_∞ is the mobility at infinite temperature. **Figure 3e** and **3f** depict the zero-field electron and hole mobilities of NA, FN, CN, and BN-based BHJ devices as a function of $1/T^2$. The FN-induced BHJ device with medium miscibility of PM/Y6 exhibits σ_h value of 7.57 meV and σ_e value of 7.90 meV. Whereas the CN-induced BHJ device with low miscibility of PM/Y6, the BN-induced BHJ device with high miscibility of PM/Y6, and the NA-based BHJ without manipulating the miscibility of PM/Y6 all present higher values (σ_h= 14.0 meV, σ_e= 13.7 meV for CN, σ_h= 11.4 meV, σ_e= 11.3 meV for BN, and σ_h= 19.7 meV, σ_e= 20.9 meV for NA). The results indicate that the density of states (DoS) in the FN-based device is narrower compared with those of the other devices. This feature is consistent with the reduced trap assisted SRH recombination, suggesting that this additive-induced miscibility control strategy can suppress both hole and electron energetic disorder in the BHJ active layer, thus less trapped states at the edge of the DoS, leading to the enhanced J_{SC} of 26.98 mA cm^{-2} and FF of 77.8%.

Conclusions

In summary, we reported a facile and effective additive-induced miscibility control approach to further prompts the PCE of the state-of-the-art PM6: Y6 system from 15.7% to 17.5%, which stands the top value for PM6: Y6 binary OSCs. We found that the additive-induced miscibility of PM6/Y6 changes lead to 1) smooth Y6 crystallization process, which reduced defects and contributed to the enhanced acceptor part photon response ; 2) hierarchical morphology with more suitable phase separation, and thereby contributed to more efficient and balanced exciton dissociation and charge collection; 3) the reduced trap-assisted SRH recombination, and therefore prolonged the carrier lifetime and suppressed the energetic disorder, contributed to the improvement of J_{SC} and FF. Our findings demonstrated that there's plenty of room at OPV morphology regulating such as the additive-induced miscibility control strategy, which paves an avenue to reach the full potential of vast existing photoactive materials.

CRediT authorship contribution statement

Jie Lv: Conceptualization and Writing-original draft. **Hua Tang:** Conceptualization and Writing-original draft. **Jiaming Huang:** Data curation. **Cenqi Yan**: Writing-review & editing. **Kuan Liu:** Data curation. **Qianguang Yang**: Data curation. **Dingqin Hu**: Data curation. **Ranbir Singh**: Writing-review & editing. **Jawon Lee**: Data curation. **Shirong Lu**: Supervision. **Gang Li:** Supervision. **Zhipeng Kan**: Conceptualization and Supervision.

Conflicts of interest

The authors declare no conflict of interest.

Acknowledgements

Z. Kan acknowledges the support from National Natural Science Foundation of China (No. 61805245) and the CAS Pioneer Hundred Talents Program (E0296102). S. Lu thanks the support from the Chongqing Funds for Distinguished Young Scientists (cstc2020jcyj-jqX0018), General Program of National Natural Science Foundation of China (62074149), and the "artificial intelligence" key project of Chongqing (cstc2017rgzn-zdyfX0030). G. Li thanks the support from Research Grants Council of Hong Kong (Project Nos 15218517, C5037-18G), Shenzhen Science and Technology Innovation Commission (Project No. JCYJ20170413154602102), the funding for Project of Strategic Importance (Project Code: 1-ZE29), and Postdoctoral Fellowships Scheme (PDFS. Code: YW3Y) provided by the Hong Kong Polytechnic University. The authors thank Mr. Huirong Su from Genuine Optronics Limited for the measurements of ellipsometry and helpful discussion on fitting of experimental data.

References

1. H. Tang, C. Yan, J. Huang, Z. Kan, Z. Xiao, K. Sun, G. Li and S. Lu, *Matter*, 2020, **3**, 1403-1432.
2. C. Yan, S. Barlow, Z. Wang, H. Yan, A. K. Y. Jen, S. R. Marder and X. Zhan, *Nat. Rev. Mater.*, 2018, **3**, 18003.
3. G. Li, W.-H. Chang and Y. Yang, *Nat. Rev. Mater.*, 2017, **2**, 17043.
4. Y. Yang, W. Chen, L. Dou, W.-H. Chang, H.-S. Duan, B. Bob, G. Li and Y. Yang, *Nat. Photon.*, 2015, **9**, 190-198.
5. G. Li, R. Zhu and Y. Yang, *Nat. Photon.*, 2012, **6**, 153-161.
6. P. Cheng, G. Li, X. Zhan and Y. Yang, *Nat. Photon.*, 2018, **12**, 131-142.
7. G. Li, V. Shrotriya, J. Huang, Y. Yao, T. Moriarty, K. Emery and Y. Yang, *Nat. Mater.*, 2005, **4**, 864-868.
8. J. Hou, O. Inganas, R. H. Friend and F. Gao, *Nat. Mater.*, 2018, **17**, 119-128.
9. J. You, L. Dou, K. Yoshimura, T. Kato, K. Ohya, T. Moriarty, K. Emery, C. C. Chen, J. Gao, G. Li and Y. Yang, *Nat. Commun.*, 2013, **4**, 1446.
10. H. Tang, H. Chen, C. Yan, J. Huang, P. W. K. Fong, J. Lv, D. Hu, R. Singh, M. Kumar, Z. Xiao, Z. Kan, S. Lu and G. Li, *Adv. Energy Mater.*, 2020, **10**, 2001076.
11. Z. Liang, J. Tong, H. Li, Y. Wang, N. Wang, J. Li, C. Yang and Y. Xia, *J. Mater. Chem A.*, 2019, **7**, 15841-15850.
12. Y. Wang, Z. Liang, X. Li, J. Qin, M. Ren, C. Yang, X. Bao, Y. Xia and J. Li, *Journal of Materials Chemistry C*, 2019, **7**, 11152-11159.
13. J. Li, N. Wang, Y. Wang, Z. Liang, Y. Peng, C. Yang, X. Bao and Y. Xia, *Sol. Energy.*, 2020, **196**, 168-176.
14. J. Yuan, Y. Zhang, L. Zhou, G. Zhang, H.-L. Yip, T.-K. Lau, X. Lu, C. Zhu, H. Peng, P. A. Johnson, M. Leclerc, Y. Cao, J. Ulanski, Y. Li and Y. Zou, *Joule*, 2019, **3**, 1140-1151.
15. Y. Cui, H. Yao, J. Zhang, K. Xian, T. Zhang, L. Hong, Y. Wang, Y. Xu, K. Ma, C. An, C. He, Z. Wei, F. Gao and J. Hou, *Adv. Mater.*, 2020, **32**, 1908205.
16. J. Wu, J. Lee, Y.-C. Chin, H. Yao, H. Cha, J. Luke, J. Hou, J.-S. Kim and J. R. Durrant, *Energy & Environ. Sci.*, 2020, **13**, 2422-2430.
17. J. Li, Y. Wang, Z. Liang, N. Wang, J. Tong, C. Yang, X. Bao and Y. Xia, *ACS. Appl. Mater. Inter.*, 2019, **11**, 7022-7029.
18. J. Li, J. Qin, X. Liu, M. Ren, J. Tong, N. Zheng, W. Chen and Y. Xia, *Sol. Energy.*, 2020, **211**, 1102-1109.
19. J. Li, Y. Wang, Z. Liang, J. Qin, M. Ren, J. Tong, C. Yang, C. Yang, X. Bao and Y. Xia, *Journal of Materials Chemistry C*, 2020, **8**, 2483-2490.
20. H. B. Naveed and W. Ma, *Joule*, 2018, **2**, 621-641.
21. L. Ye, B. A. Collins, X. Jiao, J. Zhao, H. Yan and H. Ade, *Adv. Energy Mater.*, 2018, **8**, 1703058.
22. W. Ma, J. R. Tumbleston, M. Wang, E. Gann, F. Huang and H. Ade, *Adv. Energy Mater.*, 2013, **3**, 864-872.
23. S. Pang, R. Zhang, C. Duan, S. Zhang, X. Gu, X. Liu, F. Huang and Y. Cao, *Adv. Energy Mater.*, 2019, **9**, 1901740.
24. Z. Cao, J. Chen, S. Liu, M. Qin, T. Jia, J. Zhao, Q. Li, L. Ying, Y.-P. Cai, X. Lu, F. Huang and Y. Cao, *Chem. Mater.*, 2019, **31**, 8533-8542.
25. M.-C. Michalski, J. Hardy and B. J. V. Saramago, *J. Colloid Interface Sci.*, 1998, **208**, 319-328.
26. D. K. Owens and R. C. Wendt, *J. Appl. Polym. Sci.*, 1969, **13**, 1741-1747.
27. S. Pang, R. Zhang, C. Duan, S. Zhang, X. Gu, X. Liu, F. Huang and Y. Cao, *Adv. Energy Mater.*, 2019, **9**.
28. J. Wu, G. Li, J. Fang, X. Guo, L. Zhu, B. Guo, Y. Wang, G. Zhang, L. Arunagiri, F. Liu, H. Yan, M. Zhang and Y. Li, *Nat. Commun.*, 2020, **11**, 4612.
29. D. Baran, R. S. Ashraf, D. A. Hanifi, M. Abdelsamie, N. Gasparini, J. A. Rohr, S. Holliday, A. Wadsworth, S. Lockett, M. Neophytou, C. J. Emmott, J. Nelson, C. J. Brabec, A. Amassian, A. Salleo, T. Kirchartz, J. R. Durrant and I. McCulloch, *Nat. Mater.*, 2017, **16**, 363-369.
30. D. Hu, Q. Yang, H. Chen, F. Wobben, V. M. Le Corre, R. Singh, T. Liu, R. Ma, H. Tang, L. J. A. Koster, T. Duan, H. Yan, Z. Kan, Z. Xiao and S. Lu, *Energy & Environ. Sci.*, 2020, **13**, 2134-2141.
31. J. Kettle, H. Waters, M. Horie and G. C. Smith, *J. Phys. D: Appl.*

Phys., 2016, **49**, 085601.
32. S. W. Heo, S. H. Kim, E. J. Lee and D. K. Moon, *Sol. Energy Mater. Sol. Cells*, 2013, **111**, 16-22.
33. Y. Firdaus, L. P. Maffei, F. Cruciani, M. A. Müller, S. Liu, S. Lopatin, N. Wehbe, G. O. N. Ndjawa, A. Amassian, F. Laquai and P. M. Beaujuge, *Adv. Energy Mater.*, 2017, **7**, 1700834.
34. J. Wu, G. Li, J. Fang, X. Guo, L. Zhu, B. Guo, Y. Wang, G. Zhang, L. Arunagiri, F. Liu, H. Yan, M. Zhang and Y. Li, *Nat. Commun.*, 2020, **11**, 4612.
35. H. Tang, T. Xu, C. Yan, J. Gao, H. Yin, J. Lv, R. Singh, M. Kumar, T. Duan, Z. Kan, S. Lu and G. Li, *Adv Sci (Weinh)*, 2019, **6**, 1901613.
36. C. Yan, H. Tang, R. Ma, M. Zhang, T. Liu, J. Lv, J. Huang, Y. Yang, T. Xu, Z. Kan, H. Yan, F. Liu, S. Lu and G. Li, *Adv Sci (Weinh)*, 2020, **7**, 2000149.
37. T. Liu, W. Gao, Y. Wang, T. Yang, R. Ma, G. Zhang, C. Zhong, W. Ma, H. Yan and C. Yang, *Adv. Funct. Mater.*, 2019, **29**, 1902155.
38. C. Yan, W. Wang, T.-K. Lau, K. Li, J. Wang, K. Liu, X. Lu and X. Zhan, *J. Mater. Chem A.*, 2018, **6**, 16638-16644.
39. W. Chen, T. Xu, F. He, W. Wang, C. Wang, J. Strzalka, Y. Liu, J. Wen, D. J. Miller, J. Chen, K. Hong, L. Yu and S. B. Darling, *Nano Lett.*, 2011, **11**, 3707-3713.
40. Z. Zhou, S. Xu, J. Song, Y. Jin, Q. Yue, Y. Qian, F. Liu, F. Zhang and X. Zhu, *Nat. Energy*, 2018, **3**, 952-959.
41. C. Yan, H. Tang, R. Ma, M. Zhang, T. Liu, J. Lv, J. Huang, Y. Yang, T. Xu, Z. Kan, H. Yan, F. Liu, S. Lu and G. Li, *Advanced Science*, 2020, **7**, 2000149.
42. H. Tang, C. Yan, S. Karuthedath, H. Yin, Y. Gao, J. Gao, L. Zhang, J. Huang, S. K. So, Z. Kan, F. Laquai, G. Li and S. Lu, *Sol. RRL*, 2020, **4**, 1900528.
43. T. Duan, H. Tang, R.-Z. Liang, J. Lv, Z. Kan, R. Singh, M. Kumar, Z. Xiao, S. Lu and F. Laquai, *J. Mater. Chem. A*, 2019, **7**, 2541-2546.
44. Y. Gong, Z. Kan, W. Xu, Y. Wang, S. H. AlShammari, F. Laquai, W.-Y. Lai and W. Huang, *Solar RRL*, 2018, **2**, 1800120.
45. R. Xin, J. Feng, C. Zeng, W. Jiang, L. Zhang, D. Meng, Z. Ren, Z. Wang and S. Yan, *ACS. Appl. Mater. Inter.*, 2017, **9**, 2739-2746.
46. R.-Z. Liang, M. Babics, A. Seitkhan, K. Wang, P. B. Geraghty, S. Lopatin, F. Cruciani, Y. Firdaus, M. Caporuscio, D. J. Jones and P. M. Beaujuge, *Adv. Funct. Mater.*, 2018, **28**, 1705464.
47. D. Bartesaghi, I. d. C. Pérez, J. Kniepert, S. Roland, M. Turbiez, D. Neher and L. J. A. Koster, *Nat. Commun.*, 2015, **6**, 7083.
48. Y. Liu, Y. Yang, D. Shi, M. Xiao, L. Jiang, J. Tian, G. Zhang, Z. Liu, X. Zhang and D. Zhang, *Adv. Mater.*, 2019, **31**, 1902576.
49. K. Wang, J. Lv, T. Duan, Z. Li, Q. Yang, J. Fu, W. Meng, T. Xu, Z. Xiao, Z. Kan, K. Sun and S. Lu, *ACS Appl Mater Interfaces*, 2019, **11**, 6717-6723.
50. K. Gao, S. B. Jo, X. Shi, L. Nian, M. Zhang, Y. Kan, F. Lin, B. Kan, B. Xu, Q. Rong, L. Shui, F. Liu, X. Peng, G. Zhou, Y. Cao and A. K. Y. Jen, *Adv. Mater.*, 2019, **31**, 1807842.
51. J. Lv, Y. Feng, J. Fu, J. Gao, R. Singh, M. Kumar, M. Kim, H. Tang, S. Lu, W. Zhang, I. McCulloch, J. Li and Z. Kan, *Solar RRL*, 2019, **4**, 1900403.
52. U. Albrecht and H. Bassler, *Physica Status Solidi B-Basic Research*, 1995, **191**, 455-459.

